Single mode, distributed feedback interband cascade lasers grown on Si for gas sensing

Daniel Andrés Díaz-Thomas, Diba Ayache, Maëva Fagot, Zeineb Loghmari, Audrey Gilbert, Yves Rouillard, Alexei N Baranov, Jean-Baptiste Rodriguez, Eric Tournié, A. Vicet, et al.

RESEARCH ARTICLE | JANUARY 21 2025

Single mode, distributed feedback interband cascade lasers grown on Si for gas sensing

Special Collection: Mid and Long Wavelength Infrared Photonics, Materials, and Devices

Daniel Andrés Díaz-Thomas ; Diba Ayache ; Maëva Fagot ; Zeineb Loghmari ; Audrey Gilbert ; Yves Rouillard ; Alexei N. Baranov ; Jean-Baptiste Rodriguez ; Eric Tournié ; Aurore Vicet ; Laurent Cerutti

Appl. Phys. Lett. 126, 031102 (2025)
https://doi.org/10.1063/5.0242398

Applied Physics Letters ARTICLE pubs.aip.org/aip/apl

Single mode, distributed feedback interband cascade lasers grown on Si for gas sensing

Cite as: Appl. Phys. Lett. **126**, 031102 (2025); doi: 10.1063/5.0242398
Submitted: 4 October 2024 · Accepted: 9 December 2024 ·
Published Online: 21 January 2025

View Online Export Citation CrossMark

Daniel Andrés Díaz-Thomas,[1] Diba Ayache,[1] Maëva Fagot,[1] Zeineb Loghmari,[2] Audrey Gilbert,[1] Yves Rouillard,[1] Alexei N. Baranov,[1] Jean-Baptiste Rodriguez,[1] Eric Tournié,[1,3] Aurore Vicet,[1] and Laurent Cerutti[1,a)]

AFFILIATIONS

[1]IES, University Montpellier, CNRS, F-34000 Montpellier, France
[2]mirSense, 1 Rue Jean Rostand, 91400 Orsay, France
[3]Institut Universitaire de France (IUF), F-75005 Paris, France

Note: This paper is part of the APL Special Collection on Mid and Long Wavelength Infrared Photonics, Materials, and Devices.
[a)]**Author to whom correspondence should be addressed:** laurent.cerutti@umontpellier.fr

ABSTRACT

A single mode distributed feedback (DFB) interband cascade laser (ICL) grown on a (001) Si substrate has been developed. The designed DFB ICL with a grating on top of the ridge emits at a wavelength near 3.4 μm, suited for methane gas sensing, and operates in continuous wave up to 35 °C, with a maximum output power of 4 mW/facet at 15 °C and a side mode suppression ratio of 20 dB in the whole operating range. Methane detection has been demonstrated by integrating the DFB ICL on Si with a quartz-enhanced photoacoustic spectroscopy setup, a step forward in the development of integrated photonic gas sensors on silicon platforms.

Silicon has become an essential material in the photonics industry due to its cost-effectiveness, compatibility with mature complementary metal-oxide-semiconductor (CMOS) technologies and the large size of silicon wafers. This has enabled the development of low-cost, chip-scale Si photonic integrated circuit (PIC) that meets the demands of telecom and data processing.[1] However, its application can be extended beyond the visible and near-infrared domains to the mid-infrared (MIR) spectral range (2–5 μm), paving the way for applications in spectroscopy with the development of chemical or biological sensor on chip or for free space telecommunication.[2,3]

Laser devices remain the key in this context. Despite extensive efforts to develop silicon-based lasers, the indirect bandgap of silicon and its alloys significantly reduces their efficiency and operating conditions.[4,5] However, in the last decade, there has been increasing interest in monolithically integrated III–V lasers due to their potential for high yields, low cost, and reliable manufacturing processes in mass production. The growth of III–V materials on silicon presents significant challenges due to the large lattice mismatch and the growth of polar III–V materials on non-polar substrates. This results in various types of defects such as dislocations and anti-phase boundaries (APBs). Nevertheless, much progress has been made to improve the quality of III–V materials on Si. For instance, it is possible to eliminate APBs on Si substrates by optimizing the substrate preparation and the growth conditions.[6–8]

In the telecom wavelength range, dislocations remain a significant issue as they act as non-radiative recombination centers, degrading laser performance. Therefore, it is necessary to incorporate complex dislocation filter layers to reduce their density combined with quantum dot (QD) active regions, which are more tolerant to dislocations.[9–13] In contrast, the MIR offer very elegant and simpler solutions. In fact, quantum cascade lasers (QCLs) have demonstrated very similar performance for structure grown on both Si and native substrates,[14–16] due to the sub-picosecond carrier lifetime in intersubband transition. On the other hand, type-II "W" interband cascade lasers (ICLs) have also demonstrated to be tolerant to dislocations, with the same performance for ICLs grown on different substrates, and an extrapolated lifetime of 36 years for ICLs grown on Si.[17,18] Moreover, ICLs offer lower power consumption in comparison with QCLs, which is a great advantage for their integration with Si PIC.

However, while Fabry–Pérot ICLs on Si are promising, single-mode emission remains to be demonstrated for MIR applications such as spectroscopy.[19] Although single-mode emission ICLs with distributed feedback (DFB) gratings[20–25] and slotted waveguide[26] have been

demonstrated in the wavelength range of 2.8–7 μm on both GaSb and InAs substrates, these technologies have never been implemented on lasers grown on Si emitting in the MIR.

In this work, we demonstrate a DFB ICL grown on a Si substrate and its application in quartz-enhanced photoacoustic spectroscopy (QEPAS).

The ICL heterostructure is the same as the one described in Ref. 17 and was grown by solid source molecular beam epitaxy (MBE) on a Si (001) substrate using the conditions described in Ref. 27. It consists of seven active stages designed for an emission around 3.5 μm, sandwiched between two 400 nm-thick, Te doped, GaSb separate confinement layers and between top and bottom, n-doped, InAs/AlSb superlattice-based claddings of 1.8 and 3 μm-thickness, respectively. The Fabry–Pérot laser fabricated with this ICL heterostructure grown on Si exhibited a threshold current as low as 45 mA at 20 °C in continuous wave, for 2 mm long and 8 μm narrow ridges. The spectral emission was broad, with longitudinal multimode emission. This performance is similar to that of ICLs grown on native GaSb substrates.[17,18]

Next, we designed the Bragg grating to be integrated on top of the laser ridge to fabricate the DFB ICL. In this structure, the maximum of the gain is positioned at 3.5 μm at RT in CW operation. To address the detection of methane, we targeted a wavelength of 3.404 μm, which is within the gain spectrum of this heterostructure, since ICL gain spectra are typically 220 nm broad for ICL emitting between 3 and 4 μm.[28] The Bragg grating inscribed on the laser ridge results in a periodic perturbation of the refractive index, which, in turn, induces feedback through Bragg scattering, effectively coupling the forward and backward propagating waves when the Bragg law is verified,

$$\lambda_m = 2m \cdot n_{eff} \cdot \Lambda \tag{1}$$

with λ_m the wavelength at which the coupling occurs, m the diffraction order, n_{eff} the effective refractive index of the medium, and Λ the grating period. The coupling strength between the grating and the active zone is defined by the parameter κ as follows:[29]

$$\kappa = \frac{\Delta\omega}{4c} n_{eff} + i\frac{\Delta\alpha}{4}, \tag{2}$$

where $\Delta\omega$ and $\Delta\alpha$ are the frequency and the loss difference between the main modes and c is the speed of light in vacuum. Additionally, the values of $\Delta\omega$ and $\Delta\alpha$ depend on several parameters including the distance between the grating and the active region and the depth of the grating.[30] In this study, we chose the first Bragg order ($m = 1$) for its superior coupling coefficient compared to the higher orders.[25] This choice led to a grating period of $\Lambda = 480$ nm for $n_{eff} = 3.55$ as estimated from prior experiments. To optimize the coupling, we first determined the optimal distance between the grating and the active region by finite-element numerical simulations using the COMSOL software.[31] The simulation parameters included the thickness of the top cladding and the etch depth and took into account the etching profile, since our etching conditions of the InAs/AlSb superlattice result in a trapezoidal shape with an angle of 110°. Furthermore, only the real part of κ is considered in the modeling, since the coupling loss, estimated at 0.2% of the coupling strength, remains very low.

Figure 1 shows the evolution of the coupling coefficient κ as a function of the grating etching depth for various top cladding thicknesses between 0.5 and 1.8 μm, with a duty cycle of 60%. κ increases with the grating etching depth, regardless of the top cladding thickness. To ensure a stable single mode emission over a wide range of temperatures and currents, the product κ·L, where L is the cavity length, was selected to be between 2 and 3.[29] Therefore, considering a laser cavity length of 2 mm, the coefficient κ should ideally range between 10 and 15 cm^{-1}. This range is highlighted in red in Fig. 1, which shows that the top cladding thickness should then be between 0.5 and 1 μm, with an etch depth between 0.05 and 0.5 μm.

This grating design selectively promotes two main transverse electric (TE) modes, known as semiconductor and metallic modes, which are related to the location of the electric field maximum. In order to improve the discrimination between these two modes, and therefore to enhance the single-frequency emission, the propagation losses for each mode were determined for the previously selected top cladding thicknesses. Figure 1(b) presents the evolution of the modal losses for each TE mode as a function of the grating etch depth. In these simulations, we considered only modal losses below 9 cm^{-1} to keep a low threshold current at room temperature (RT), which narrows down the choice of the top cladding thickness to the 0.7–1 μm range.

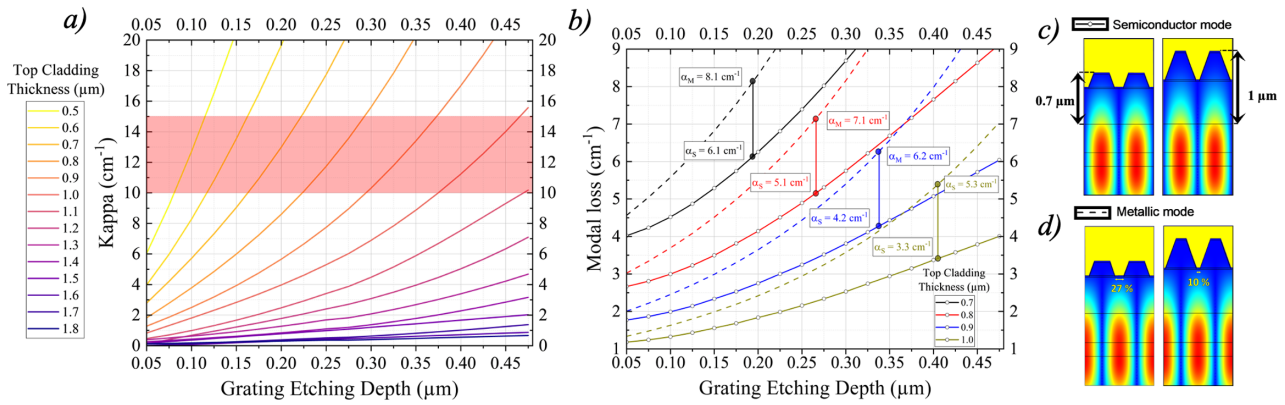

FIG. 1. (a) Evolution of the coupling coefficient (κ) as a function of grating etching depth for various top cladding thicknesses ranging from 0.5 to 1.8 μm. (b) Evolution of the TE optical mode losses with the grating etch depth. Cross sections showing the semiconductor mode (c) and metallic mode (d) for two top cladding thicknesses, 0.7 and 1 μm, with corresponding grating etching depths of 193 and 405 nm, respectively.

For both modes, the losses increase exponentially with the grating etching depth. However, this behavior is less pronounced with thicker top claddings, due to the weaker interaction between the optical mode and the grating. To achieve single mode emission, the modal losses difference $\Delta\alpha$ between the two modes should be high enough to promote only one mode. For shallow grating etching depths, $\Delta\alpha$ is low, making it difficult to favor one mode over the other, while deeper etching depths introduce significant optical losses. We selected a value of $\Delta\alpha = 2\,\mathrm{cm}^{-1}$, similar to that used by Ning *et al.*,[25] for each top cladding thickness, which allowed to determine the minimum etching depth of the grating that ensures single mode emission.

Figures 1(c) and 1(d) show the simulated cross sections of two periods of the gratings for two cladding thickness of 0.7 and 1 μm, with corresponding grating etching depths of 193 and 405 nm, respectively. Figure 1(c) represents the semiconductor mode, with the field intensity maximum located below the semiconductor region, while Fig. 1(d) represents the metallic mode, with the field intensity peaking below the metal layer. As indicated in Fig. 1(d), the metallic surface area overlapped by the metallic mode decreases from 27% for a top cladding of 0.7 μm (193 nm etch depth) to 10% for a top cladding of 1 μm (405 nm etch depth). As a compromise, a cladding thickness of 0.8 μm was chosen, resulting in a grating etch depth of 260 nm. This geometry results in a 23% overlap between the metal and the optical mode. Altogether, our design giving κ between 10 and 15 cm^{-1}, $\Delta\alpha$ around 2 cm^{-1}, and optical losses induced by the grating around 5 cm^{-1} with a 60% duty cycle, imposes a top cladding thickness around 0.8 μm and a grating etch depth around 260 nm.

The initial top cladding thickness of the epitaxial ICL structure being 1.8 μm, the first step in the fabrication process for the DFB was to etch the entire surface to reduce the top cladding thickness down to 0.8 μm. This was done by an inductively coupled plasma reactive ion etching (ICP-RIE) using a Cl_2-Ar chemistry. The DFB grating was then patterned on a resist by electron beam lithography (EBL) and transferred to the InAs/AlSb top cladding using Cl_2-based ICP-RIE. The inset in Fig. 2 shows the trapezoidal profiles of the DFB grating after the etching step, which was taken into account in the modeling. To support only the fundamental transverse mode and ensure single transverse mode emission, 4.5 μm wide ridges were processed by standard photolithography and dry etching. The ridge was defined down to the top of the bottom cladding, where the bottom contact is taken. The electrical insulation and planarization layers were achieved by baking the photoresist at 200 °C for 2 h. Ti-Au was then deposited for both the top and bottom contacts. The Si substrate was then mechanically thinned down to 100 μm, and the processed wafer was cleaved with an automatic scriber (S100 from JFP Microtechnic) to form uncoated 2-mm-long cavities soldered epitaxial side up with indium onto Al_2O_3 heatsinks. Figure 2 displays a scanning electron microscope (SEM) image of a fully processed DFB ICL grown on a Si substrate.

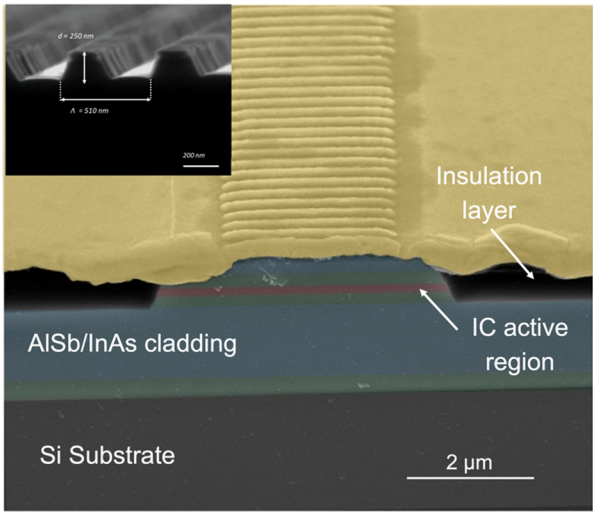

FIG. 2. False color SEM image of a fully processed DFB-ICL grown on Si. Inset: SEM image of the DFB grating after dry etching.

Figure 3(a) shows the P-I-V curve in CW of a representative DFB ICL grown on Si as a function of the temperature. The laser operates in CW up to 35 °C. At 15 °C, the threshold current and the maximum output power were 40 mA and 3.7 mW/facet, respectively. The slope efficiency (per facet) amounts to 0.09 W/A, while the external differential quantum efficiency (related to the two facets) is defined as

$$\eta_d = \frac{q}{h\nu}\frac{\Delta P}{\Delta I}, \tag{3}$$

with q the electron charge, h the Planck's constant, and ν the frequency of light is around 50%. This value is considerably lower than the 120%–170% reported for Fabry–Pérot ICLs fabricated from the same heterostructure.[17] This is probably due to the relatively strong coupling ($\kappa \cdot L \sim 2$) and the large detuning with respect to the gain peak, which both decrease the output power and efficiency. This performance suggests that the DFB modes have higher losses and calls for further work to refine the design parameters and fabrication steps and reduce these losses.

Figure 3(b) presents the emission spectra taken at 15 °C for several injection currents between 50 and 110 mA. Single mode operation with at least 20 dB SMSR was achieved over the whole current range. Furthermore, this DFB ICL exhibited single-frequency operation in the continuous-wave regime over the whole test temperature range, from 10 to 30 °C. From these measurements, the tuning range associated with the temperature and the current is 0.28 nm/°C and 0.14 nm/mA, respectively. The temperature tunability is consistent with DFB ICLs grown on GaSb,[21,25,32] while the current tunability is an order of magnitude higher. This effect is related to the higher series resistance, which implies a larger Joule heating effect and thus a higher wavelength tuning. This large tunability offers accurate wavelength control for gas spectroscopy.

Figure 4 shows the evolution of the emission peak wavelength as a function of the current for the various temperatures. Isolated longitudinal mode hops are observed around 80 mA at 10 °C and 100 mA at 15 °C. However, by carefully adjusting both the current and the temperature, single-mode operation can be maintained over the whole 3.402–3.414 μm wavelength range, which translates into a wavenumber tuning range as large as 11 cm^{-1}.

This DFB ICL grown on Si was then used for gas detection using quartz enhanced photoacoustic spectroscopy (QEPAS).[33] The laser was operated at 10 °C to cover the absorption lines of the methane (CH_4) at 3.402 and 3.404 μm, a gas of great interest for environmental and defense applications.[34] Figure 5(a), which presents the absorption lines of CH_4 obtained from the HITRAN Database[35] at ambient

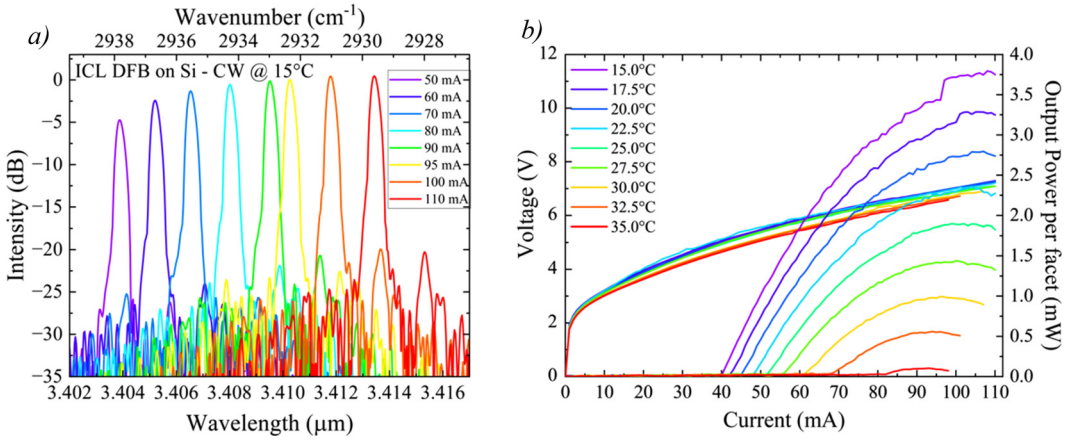

FIG. 3. (a) P-I-V curve of the DFB ICL in CW at different temperature. (b) Emission spectra of the DFB ICL grown on Si in CW at 15 °C for different current injection.

temperature and atmospheric pressure with a path length of 2 cm and a concentration of 1 ppmv, together with the laser mode wavelength at 10 °C for various drive currents, shows a good overlap between the absorption lines and the laser emission. For the gas sensing demonstration, the laser wavelength was tuned across the CH_4 absorption lines at a frequency of $\frac{f_0}{2} = 16\,382$ Hz and a modulation amplitude of 20 mA. A calibrated concentration of 400 ppmv of CH_4 was used to perform this proof of concept.

Figure 5(b) shows the 2f (second harmonic) QEPAS signal, obtained by wavelength modulation. It is proportional to the second derivative of the gas absorption, measured with a time constant of 200 ms after demodulation by the lock-in amplifier for the methane absorption lines between 2937 and 2939 cm^{-1}. A small shift in the position of the main peak can be observed due to the non-linearity of the tuning rate. The QEPAS signal drops abruptly above 2937.3 cm−1 when the laser emission reaches a mode hop. The amplitude of the signal obtained on the intense CH_4 absorption line of located at 2938.2 cm^{-1} can be used to determine the limit of detection (LOD) of the sensor, defined as the minimum gas concentration that the sensor can detect (signal to noise ratio SNR = 1). The SNR is evaluated on the signal considering the noise standard deviation (0.025 mV). Here, the SNR is equal to 56 with a time constant τ of 200 ms, and the LOD of the sensor is then estimated as

$$\mathrm{LOD}(\tau) = \frac{400}{\mathrm{SNR}\,(\tau)} = 7\ \mathrm{ppmv}, \tag{4}$$

limited by the laser power in the QEPAS cell, around 1 mW in our experimental conditions.

To summarize, in this work, we have demonstrated a single mode ICL grown on Si substrate and used it for CH_4 detection using QEPAS measurement. This was achieved by careful design and fabrication of the Bragg grating inscribed in the ICL ridge. The DFB-ICL operated in CW up to 35 °C with a threshold current of 40 mA and a maximum output power of 3.7 mW at 15 °C. The emission was single mode over

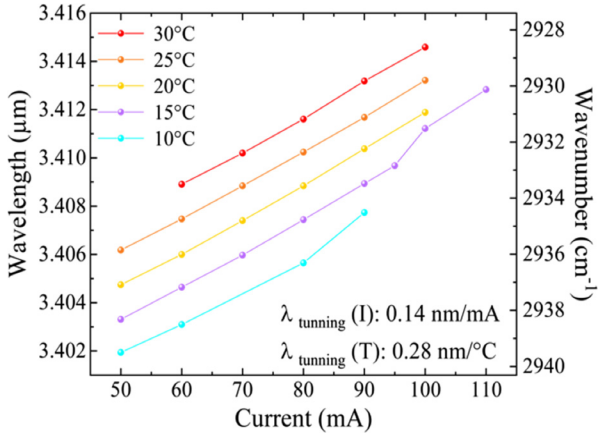

FIG. 4. Temperature and current tuning of the DFB ICL grown on Si at various temperatures between 10 and 30 °C.

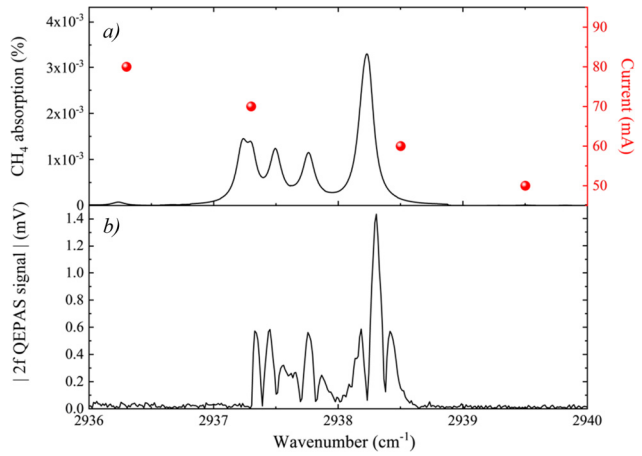

FIG. 5. (a) Absorption lines of CH_4 obtained from the HITRAN Database at ambient temperature and atmospheric pressure with a path length of 2 cm and a concentration of 1 ppmv (black lines). Laser peak emission at 10 °C and different drive current (red dots). (b) 2f QEPAS signal obtained for a concentration of 400 ppmv of CH_4.

the whole operating range with a SMSR higher than 20 dB and a 12 nm, translating in a 11 cm^{-1}, continuous tunability. The single mode emission, tailored to overlap the CH_4 absorption lines near 3.404 μm, allowed demonstrating gas detection by QEPAS, with a limit of detection of 7 ppmv, limited by the laser power in the QEPAS cell. By optimizing the heterostructure design to better match the position of the gain peak and the target spectroscopy line, and by further improving the coupling parameters, the laser output power can be largely increased, and the sensor performance much improved. This demonstration of a single mode ICL grown on Si for gas spectroscopy is a step toward the realization of an optical gas sensor on Si PIC.

The authors acknowledge funding from the France 2030 program (ANR-11-EQPX0016, ANR-21-ESRE-0026), the French Occitanie Region (LASIDO project), the French Agency for Defense and Innovation (AID-DGA), and the BPI (HyQuality Project DOS0188007/00A).

AUTHOR DECLARATIONS

Conflict of Interest

The authors have no conflicts to disclose.

Author Contributions

Daniel Andrés Díaz-Thomas: Conceptualization (equal); Data curation (equal); Formal analysis (equal); Investigation (equal); Methodology (equal); Writing – original draft (equal). **Diba Ayache:** Formal analysis (equal); Investigation (equal); Methodology (equal); Resources (equal); Writing – original draft (equal). **Maëva Fagot:** Resources (equal). **Zeineb Loghmari:** Resources (equal). **Audrey Gilbert:** Resources (equal). **Yves Rouillard:** Resources (equal). **Alexei N. Baranov:** Resources (equal). **Jean-Baptiste Rodriguez:** Resources (equal). **Eric Tournié:** Funding acquisition (equal); Project administration (equal); Resources (equal); Writing – review & editing (equal). **Aurore Vicet:** Formal analysis (equal); Funding acquisition (equal); Methodology (equal); Project administration (equal); Resources (equal); Writing – review & editing (equal). **Laurent Cerutti:** Conceptualization (equal); Formal analysis (equal); Funding acquisition (equal); Investigation (equal); Methodology (equal); Project administration (equal); Resources (equal); Supervision (equal); Writing – review & editing (equal).

DATA AVAILABILITY

The data that support the findings of this study are available from the corresponding author upon reasonable request.

REFERENCES

[1]Y. Shi, Y. Zhang, Y. Wan *et al.*, "Silicon photonics for high-capacity data communications," Photonics Res. **10**(9), A106 (2022).
[2]O. Spitz, P. Didier, L. Durupt *et al.*, "Free-space communication with directly modulated mid-infrared quantum cascade devices," IEEE J. Sel. Top. Quantum Electron. **28**(1), 1–9 (2022).
[3]P. Didier, H. Knötig, O. Spitz *et al.*, "Interband cascade technology for energy-efficient mid-infrared free-space communication," Photonics Res. **11**(4), 582 (2023).
[4]R. E. Camacho-Aguilera, Y. Can, N. Patel *et al.*, "An electrically pumped germanium laser," Opt. Express **20**(10), 11316 (2012).
[5]B. Marzban, L. Seidel, T. Liu *et al.*, "Strain engineered electrically pumped SiGeSn microring lasers on Si," ACS Photonics **10**(1), 217–224 (2023).
[6]M. Rio Calvo, J.-B. Rodriguez, C. Cornet *et al.*, "Crystal phase control during epitaxial hybridization of III-V semiconductors with silicon," Adv Electron. Mater. **8**(1), 2100777 (2022).
[7]K. Li, J. Yang, Y. Lu *et al.*, "Inversion boundary annihilation in GaAs monolithically grown on on-axis silicon (001)," Adv. Opt. Mater. **8**(22), 2000970 (2020).
[8]A. Gilbert, M. Ramonda, L. Cerutti *et al.*, "Epitaxial growth of III-Vs on on-axis Si: Breaking the symmetry for antiphase domains control and burying," Adv. Opt. Mater. **11**(15), 2203050 (2023).
[9]C. Shang, J. Selvidge, E. Hugues *et al.*, "A pathway to thin GaAs virtual substrate on on-axis Si (001) with ultralow threading dislocation density," Phys. Status Solidi A **218**(3), 2000402 (2021).
[10]M. Buffolo, L. Rovere, C. De Santi *et al.*, "Degradation of 1.3 μm InAs quantum-dot laser diodes: Impact of dislocation density and number of quantum dot layers," IEEE J. Quantum Electron. **57**(1), 1–8 (2021).
[11]J. Selvidge, E. T. Hugues, J. C. Norman *et al.*, "Reduced dislocation growth leads to long lifetime InAs quantum dot lasers on silicon at high temperatures," Appl. Phys. Lett. **118**(19), 192101 (2021).
[12]C. Shang, E. Hugues, Y. Wan *et al.*, "High-temperature reliable quantum-dot lasers on Si with misfit and threading dislocation filters," Optica **8**(5), 749 (2021).
[13]E. T. Hughes, C. Shang, J. Sevidge *et al.*, "Gradual degradation in InAs quantum dot lasers on Si and GaAs," Nanoscale **16**(6), 2966–2973 (2024).
[14]H. Nguyen-Van, A. N. Baranov, Z. Loghmari *et al.*, "Quantum cascade lasers grown on silicon," Sci. Rep. **8**(1), 7206 (2018).
[15]Z. Loghmari, J.-B. Rodriguez, A. N. Baranov *et al.*, "InAs-based quantum cascade lasers grown on on-axis (001) silicon substrate," APL Photonics **5**(4), 041302 (2020).
[16]S. Xu, S. Zhang, J. D. Kirch *et al.*, "8.1 μm-emitting InP-based quantum cascade laser grown on Si by metalorganic chemical vapor deposition," Appl. Phys. Lett. **123**(3), 031110 (2023).
[17]L. Cerutti, D. A. Díaz Thomas, J.-B. Rodriguez *et al.*, "Quantum well interband semiconductor lasers highly tolerant to dislocations," Optica **8**(11), 1397 (2021).
[18]M. Fagot, D. A. Díaz Thomas, A. Gilbert *et al.*, "Interband cascade lasers grown simultaneously on GaSb, GaAs and Si substrates," Opt. Express **32**(7), 11057 (2024).
[19]T. Hu, B. Dong, X. Luo *et al.*, "Silicon photonic platforms for mid-infrared applications [Invited]," Photonics Res. **5**(5), 417 (2017).
[20]R. Weih, L. Nähle, S. Höfling *et al.*, "Single mode interband cascade lasers based on lateral metal gratings," Appl. Phys. Lett. **105**(7), 071111 (2014).
[21]C. S. Kim, M. Kim, J. Abell *et al.*, "Mid-infrared distributed-feedback interband cascade lasers with continuous-wave single-mode emission to 80 °C," Appl. Phys. Lett. **101**(6), 061104 (2012).
[22]Y. Jiang, L. Li, H. Ye *et al.*, "InAs-based single-mode distributed feedback interband cascade lasers," IEEE J. Quantum Electron. **51**(9), 1–7 (2015).
[23]J. Scheuermann, R. Weih, M. von Eldinger *et al.*, "Single-mode interband cascade lasers emitting below 2.8 μm," Appl. Phys. Lett. **106**(16), 161103 (2015).
[24]F. Xie, M. Stocker, J. Pham *et al.*, "Distributed feedback interband cascade lasers with top grating and corrugated sidewalls," Appl. Phys. Lett. **112**(13), 131102 (2018).
[25]C. Ning, R.-X. Sun, S.-M. Liu *et al.*, "GaSb surface grating distributed feedback interband cascade laser emitting at 3.25 μm," Opt. Express **30**(16), 29007 (2022).
[26]J. A. M. Fordyce, D. A. Diaz-Thomas, L. O'Faolain *et al.*, "Single-mode interband cascade laser with a slotted waveguide," Appl. Phys. Lett. **121**(21), 211102 (2022).
[27]M. Rio Calvo, L. Monge Bartolomé, M. Bahriz *et al.*, "Mid-infrared laser diodes epitaxially grown on on-axis (001) silicon," Optica **7**(4), 263 (2020).
[28]K. Ryczko, A. Zielińska, and G. Sęk, "Interband cascade active region with ultra-broad gain in the mid-infrared range," Materials **14**(5), 1112 (2021).
[29]H. Kogelnik and C. V. Shank, "Coupled-wave theory of distributed feedback lasers," J. Appl. Phys. **43**(5), 2327–2335 (1972).
[30]M. Carras, M. Garcia, X. Marcadet *et al.*, "Top grating index-coupled distributed feedback quantum cascade lasers," Appl. Phys. Lett. **93**(1), 011109 (2008).
[31]See www.comsol.com for COMSOL Multiphysics®. v. 6.2 (COMSOL AB, Stockholm, Sweden).

[32]S. Forouhar, C. Borgentun, C. Frez *et al.*, "Reliable mid-infrared laterally-coupled distributed-feedback interband cascade lasers," Appl. Phys. Lett. **105**(5), 051110 (2014).
[33]A. A. Kosterev, Y. A. Bakhirkin, R. F. Curl, and F. K. Tittel, "Quartz-enhanced photoacoustic spectroscopy," Opt. Lett. **27**(21), 1902 (2002).
[34]T. Liang, S. Qiao, Y. Chen *et al.*, "High-sensitivity methane detection based on QEPAS and H-QEPAS technologies combined with a self-designed 8.7 kHz quartz tuning fork," Photoacoustics **36**, 100592 (2024).
[35]I. E. Gordon, L. S. Rothman, C. Hill *et al.*, "The HITRAN2016 molecular spectroscopic database," J. Quant. Spectrosc. Radiat. Transfer **203**, 3–69 (2017).